

Cherif, Hiba; Ghomrassi, Anissa; Sghaier, Jalila; Mhiri, Hatem; Bournot, Philippe

Article

A receiver geometrical details effect on a solar parabolic dish collector performance

Energy Reports

Provided in Cooperation with:

Elsevier

Suggested Citation: Cherif, Hiba; Ghomrassi, Anissa; Sghaier, Jalila; Mhiri, Hatem; Bournot, Philippe (2019) : A receiver geometrical details effect on a solar parabolic dish collector performance, Energy Reports, ISSN 2352-4847, Elsevier, Amsterdam, Vol. 5, pp. 882-897, <https://doi.org/10.1016/j.egy.2019.07.010>

This Version is available at:

<https://hdl.handle.net/10419/243636>

Standard-Nutzungsbedingungen:

Die Dokumente auf EconStor dürfen zu eigenen wissenschaftlichen Zwecken und zum Privatgebrauch gespeichert und kopiert werden.

Sie dürfen die Dokumente nicht für öffentliche oder kommerzielle Zwecke vervielfältigen, öffentlich ausstellen, öffentlich zugänglich machen, vertreiben oder anderweitig nutzen.

Sofern die Verfasser die Dokumente unter Open-Content-Lizenzen (insbesondere CC-Lizenzen) zur Verfügung gestellt haben sollten, gelten abweichend von diesen Nutzungsbedingungen die in der dort genannten Lizenz gewährten Nutzungsrechte.

Terms of use:

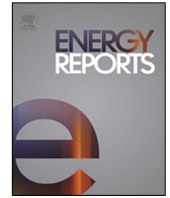
Documents in EconStor may be saved and copied for your personal and scholarly purposes.

You are not to copy documents for public or commercial purposes, to exhibit the documents publicly, to make them publicly available on the internet, or to distribute or otherwise use the documents in public.

If the documents have been made available under an Open Content Licence (especially Creative Commons Licences), you may exercise further usage rights as specified in the indicated licence.



<https://creativecommons.org/licenses/by-nc-nd/4.0/>



Research paper

A receiver geometrical details effect on a solar parabolic dish collector performance



Hiba Cherif^{a,*}, Anissa Ghomrassi^a, Jalila Sghaier^a, Hatem Mhiri^a, Philippe Bournot^b

^a Unit of Thermal and Thermodynamics in Industrial Processes, National Engineering School of Monastir, Monastir 5000, Tunisia

^b IUSTI, UMR CNRS 6595, Technopole de Château-Gombert, 5 Rue Enrico Fermi, Marseille 13013, France

ARTICLE INFO

Article history:

Received 10 September 2018

Received in revised form 7 June 2019

Accepted 9 July 2019

Available online xxxx

Keywords:

Parabolic dish

Receiver

Solar heat flux distribution

Temperature distribution

ABSTRACT

In the present study, a parametric study of a parabolic dish receiver system is investigated in order to determine the best configuration to achieve an optimal system performance.

A series of numerical simulations has been conducted for four receiver tubes and two positions of the receiver inlet/outlet configurations: position 1 and position 2.

The thermal analysis proves that the receiver's inlet/outlet configuration effect is influenced by the geometric properties of the receiver.

Numerical results show that with a “low” height receiver ($H = 0.075$ m, $H = 0.048$ m), position 2 gives the highest thermal efficiency, while position 1 ensures the greatest thermal efficiency value for the “elevated” height cylindrical receiver ($H = 1.2$ m, $H = 0.468$ m).

Indeed, for the configuration with $H = 0.075$ m, the thermal efficiency increases by 62.6% from position 1 to 2. Moreover, by changing the position from 1 to 2, the thermal efficiency decreases by 53% for a configuration with $H = 1.2$ m.

© 2019 Published by Elsevier Ltd. This is an open access article under the CC BY-NC-ND license (<http://creativecommons.org/licenses/by-nc-nd/4.0/>).

1. Introduction

Renewable energies have gained more and more interest in recent years (Zhang et al., 2018) for numerous reasons such as the increase of fossil fuels' prices, the high concentration of CO₂ emissions, the need to reduce greenhouse gas emissions and the growing worldwide energy consumption. It is a form of inexhaustible energy whose consumption does not use up resources in nature. One of the most important renewable energy sources available today is solar energy. It is a very abundant clean energy source that emits no greenhouse gases. For this reason, several researchers are interested in this energy form (Furler et al., 2012; Mills, 2004; Badran et al., 2010).

The incident solar radiation is captured by the solar thermal collectors and converted into useful energy such as electricity (Li et al., 2011).

The concentrating solar collectors are the most developed technology for the use of solar energy owing to their higher temperatures in the focal zone. The most well-known technologies for concentrating solar collectors are solar power towers, solar parabolic dishes, parabolic trough collectors and linear Fresnel reflectors (Li et al., 2011; Luo et al., 2018; Ghomrassi et al., 2015; Sharma et al., 2016). Solar dish collectors are gaining more

and more interest thanks to their high temperature in the focal point and their best concentration ratio in all four types. They are frequently used to concentrate the incident solar radiation in order to heat a working fluid at medium or high temperatures namely solar hydrogen production (Furler et al., 2012), Dish-Stirling system (Mills, 2004) and solar cooker (Badran et al., 2010).

According to the literature, a wide variety of studies investigates experimentally or numerically the solar parabolic dish (Steinfeld and Schubnell, 1993; Johnston, 1998; Shuai et al., 2008; Daly, 1979; Shuai et al., 2010; Khanna et al., 2013; Khanna and Sharma, 2016; Huang and Yu, 2018; Huang et al., 2018; Collado et al., 1986). The authors focused on the improvement of the solar concentrating systems' optical performance.

To estimate the optical performance of the latter, it is required to measure the focal flux distribution. Experimentally, it is difficult to predict the solar flux distribution concentrated on the focal point of the parabolic dish. That is why, a numerical modeling of the solar concentration system has been used.

The Monte-Carlo ray-tracing method is frequently used in the solar energy field to determine the concentrated solar heat flux and optical energy distribution (Steinfeld and Schubnell, 1993; Johnston, 1998; Shuai et al., 2008; Daly, 1979; Shuai et al., 2010). It consists in developing a numerical code which has been used by many researchers (Johnston, 1998; Shuai et al., 2008; Daly, 1979).

Steinfeld and Schubnell (1993) have used this method to study the sunshape influence on the optimal parameters of a cavity

* Corresponding author.

E-mail address: hiba.cherif@yahoo.fr (H. Cherif).

Nomenclature

a	Absorption coefficient
A_s	Receiver surface area (m^2)
C	Linear anisotropic phase function coefficient
C_p	Specific heat capacity ($kJ\ kg^{-1}\ K^{-1}$)
C_s	Concentration ratio
D	Absorber tube diameter (m)
H	Absorber tube length (m)
I	Direct normal irradiance (DNI) ($W\ m^{-2}$)
k	Turbulent kinetic energy ($m^2\ s^{-2}$)
\dot{m}	Mass flow rate of working fluid (kg/s)
n	Medium refractive index
P	Static pressure (Pa)
Re	Reynolds number
S_g	User defined radiation source
S_h	Source term for the energy equation ($J\ m^{-3}\ s^{-1}$)
T	Temperature (K)
u, v, w	x, y, z velocity components ($m\ s^{-1}$)
x, y, z	Cartesian coordinates (m)

Greek symbol

δ_{ij}	Kronecker delta function
ε	Turbulent dissipation rate ($m^2\ s^{-3}$)
μ	Dynamic viscosity ($kg\ m^{-1}\ s^{-1}$)
η_{th}	Thermal efficiency
ρ	Density ($kg\ m^{-3}$)
σ	Stefan Boltzmann constant
σ_s	Scattering coefficient
λ	Thermal conductivity ($W\ m^{-1}\ K^{-1}$)

Abbreviations

CFD	Computational Fluid Dynamics
NSE	Navier–Stokes Equations

receiver in a solar parabolic dish. Similarly, a numerical model of a solar dish collector was investigated by [Shuai et al. \(2008\)](#), in which the sunshape and surface slope error effects have been studied using the Monte-Carlo ray-tracing method. Another study is carried out by [Shuai et al. \(2010\)](#), in which they have applied the experimental and numerical study using the Monte Carlo ray-tracing method to evaluate the solar heat flux distribution on the focal plane of the parabolic solar collector and on the wall of the receiver's cavity.

In addition to the Monte Carlo ray tracing method, analytical equations are also used in other studies. In fact, [Khanna et al. \(2013\)](#) have analytically assessed the absorbed flux function on a bent absorber tube taking into account circumferential and axial variations. Optical errors and Gaussian sun shape have also been integrated. In another study of [Khanna and Sharma \(2016\)](#), an explicit analytical expression is derived to find the solar flux distribution on an undeflected absorber tube of a parabolic trough concentrator accounting for the sun-shape and optical errors. [Huang and Yu \(2018\)](#) have proposed a new heat flux distribution function resulting from the convolution of the heliostat image function with the solar flux distribution. These authors have also presented analytically the solar flux distribution on the image

plane of a round spherical heliostat in another work ([Huang et al., 2018](#)). This analytical method is validated by both the ray tracing and numerical method.

[Collado et al. \(1986\)](#) have established an analytical function for the heat flux distribution due to a rectangular heliostat focused on the receiver plane of a solar power tower.

However, all these authors have treated only the optical behavior without studying the thermal behavior in the presence of a heat transfer fluid.

The next part of the works focuses on the study of various receiver shapes and their thermal behavior.

[Tan et al. \(2014\)](#) were interested in studying a semi-spherical cavity receiver applied for the parabolic dish collector. They conducted an experimental study to estimate its heat loss. Different fluid inlet temperatures, receiver inclination angles and aperture sizes were studied in order to develop experimental correlations for Nusselt number as a function of Grashof number.

[Reddy et al. \(2016\)](#) examined a solar dish collector with a modified cavity receiver. They carried out a numerical investigation to determine the influence of wind characteristics, receiver configuration and receiver orientation on the receiver heat loss. They proposed a correlation of Nusselt number as a function of wind effects to estimate the combined convection heat losses from the receiver. Moreover, [Azzouzi et al. \(2017\)](#) presented an experimental and analytical study to investigate the effect of various parameters on the thermal efficiency and total heat loss of the cylindrical cavity receiver for a parabolic solar concentrator. In another work, [Sarwar et al. \(2015\)](#) conducted a numerical and experimental study to investigate the aperture size effects on the steady-state temperatures of a cylindrical solar receiver throughout the day.

A numerical study was developed by [Daabo et al. \(2016\)](#), in which three different geometries of a cavity receiver: cylindrical, conical and spherical in solar dish collectors were optically studied. They concluded that the conical shape was the most beneficial compared to the other two shapes.

Furthermore, [Yu et al. \(2015\)](#) conducted an experimental study to investigate the concentrated solar heat flux and temperature distributions of a steel plate receiver. The obtained results have been compared to numerical outcomes investigated by the commercial software FLUENT. Similarly, [Roldan et al. \(2013\)](#) have experimentally and numerically illustrated the temperature distribution of the receiver tube. Another study is carried out by [Wang et al. \(2012\)](#), in which they have numerically determined the temperature distribution of the receiver tube for different materials.

In another investigation of [Khanna et al. \(2016\)](#), an explicit expression is derived to find the temperature distribution of bimetallic absorber tube of a parabolic trough concentrator taking into account the Gaussian sun-shape and the optical errors 'system.

The non-uniform temperature distribution can lead to bending/deformation of a receiver. [Khanna and Sharma \(2015\)](#) have dealt with this topic and an analytical expression has been made in order to find the bending in the receiver tube of the parabolic trough and the results were compared with the experimental measurement. Bending/Deformation can occur in the receivers of the parabolic trough, parabolic dish and Fresnel reflector.

Moreover, [Wang and Siddiqui \(2010\)](#) conducted a numerical study using the commercial FEMAP software which analyzed different geometric parameters' effects such as the aperture size, inlet/outlet configuration of the solar receiver and the parabolic dish rim angle. These authors have tested a fixed aspect ratio ($\frac{\text{receiver diameter}}{\text{receiver height}}$) with several fluid inlet /outlet positions and concluded that the configuration of tangential inlet located at the top with a tangential outlet located at the bottom is the configuration that ensures the best thermal performance.

In the present work, by keeping the receiver volume constant, we study different aspect ratios. We take the same configuration of Mo Wang and we examine if the same result obtained by Wang and Siddiqui (2010) is valid for different receiver aspect ratios.

The novelty of our work is to expand these results for different heights and diameters of the receiver and determine its limits and areas of validity.

In order to carry out this study, the SOLTRACE software is used to predict the concentrated solar heat flux distribution and the FLUENT code to predict the receiver's thermal performance. This coupled method is used by Li et al. (2011).

First, the configuration of Yu et al. (2015) is taken into consideration in order to validate our numerical results carried out using the commercial CFD FLUENT code with experimental results of Tao Yu et al.

Then, the cylindrical receivers are designated, keeping the same cylinder volume of Wang and Siddiqui (2010), by varying their height and diameter, and two different configurations of inlet/outlet are carried out in order to verify the result found and discussed by Wang and Siddiqui (2010).

The first tested configuration (position 1) consists of a tangential inlet located at the top with a tangential outlet located at the bottom. The second configuration (position 2) is a tangential inlet located at the bottom with a normal outlet on the top surface.

2. Material and methods

In this section, we take the same configuration of Yu et al. (2015) in order to investigate the thermal performance of a parabolic dish by a numerical simulation.

First, the SOLTRACE software is used to calculate the concentrated solar heat flux densities. The calculated densities are, then, introduced into the FLUENT software as thermal boundary conditions for the receiver wall through UDF. Using a numerical simulation and taking into account certain simplifying assumptions and boundary conditions, it is possible to investigate the thermal characteristics of the receiver.

2.1. Calculation of the solar heat flux by SOLTRACE

SOLTRACE (Wendelin et al., 2013) is a software tool developed at the National Renewable Energy Laboratory (NREL) commonly used in the solar energy field to model the concentrated solar power systems and analyze their optical performance.

The execution of the model in SOLTRACE comprises several steps:

- Definition of the sun shape and direction.
- Input of the optical properties that will be connected with the optical elements of the system.
- Definition of the system geometry that is made up of stages, and each stage of elements.
- The choice of the rays' number to be traced.
- The extraction of results.

In SolTrace, a system is organized into stages in a global coordinate system. A stage is clearly defined as a section of the geometry that is sequentially hit by rays propagating from the sun to the final receiver. A complete system geometry may comprise one or more stages. The target for this organization is to use an efficient tracing to limit the computing time (Garcia et al., 2008).

In our case, the solar parabolic dish is formed by two stages: the reflector defines the first stage and the receiver is the second stage.

A stage is composed of "elements". It may comprise one or more elements. Each element is defined by a surface, an optical

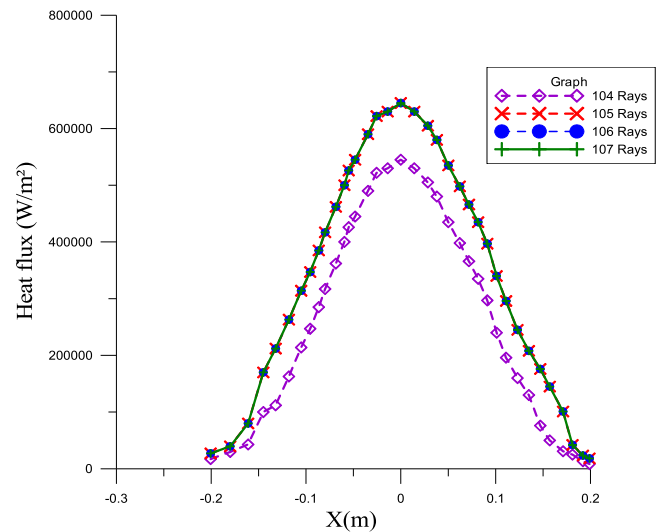


Fig. 1. Rays numbers effect on heat flux distribution.

interacting type and a set of optical properties. The location and orientation of the stages are specified in the global coordinate system, while the location and orientation of the elements are defined in the coordinate system related to its stage (Jafrancesco et al., 2018).

In our case, each stage is composed of one element.

The sun shape and direction are firstly defined. Three options are available; pillbox, Gaussian and user-defined profiles. In the present study, a Gaussian sun shape is supposed and a direct normal irradiation of 663.4 W/m^2 is considered, the same direct normal irradiation (Yu et al., 2015).

Then, the optical properties of each element are defined. In this case, reflectivity, transmissivity, slope error, specular error, error type and refraction indices are properties defined for every element.

Thereafter, the parabolic solar concentrator geometry including the stage definitions is created. The reflector defines the first stage and the receiver is the second stage. The two stages are each composed of one element.

Each stage will be defined by a set of stage properties, position and orientation information in the global coordinate system.

After defining the system, the number of rays to be traced through the system is chosen according to the details needed in the results. For example, optical efficiency information can be obtained with fewer rays than needed for a detailed concentrated solar heat flux. In general, ray numbers of about 10^6 are required for concentrated solar heat flux distribution.

Our results are focused on the study of concentrated solar heat flux distribution. For this reason, ray numbers on the order of one million are required for flux mapping.

A ray's number sensitivity study is performed in order to ensure the independence of the solar heat flux distribution from the rays' number.

Four rays' numbers are tested: 10^4 , 10^5 , 10^6 , and 10^7 . Fig. 1 shows the solar heat flux distributions on the receiver tube for different rays numbers tested. The results showed that the numbers of rays 10^5 , 10^6 and 10^7 give similar results. In contrast, the rays' number 10^4 gives a different solar heat flux distribution. So, the choice of 10^5 rays' number for all simulations was based on appreciable computing time saving compared to 10^6 and 10^7 .

The parabolic concentrator and receiver's geometry are shown in Fig. 2. The solar parabolic dish is a one surface reflector made by aluminum mirror characterized by an overall reflectivity of 0.92 and transmissivity of 0.08. Its geometric parameters and optical properties are presented in Table 1 from (Yu et al., 2015).

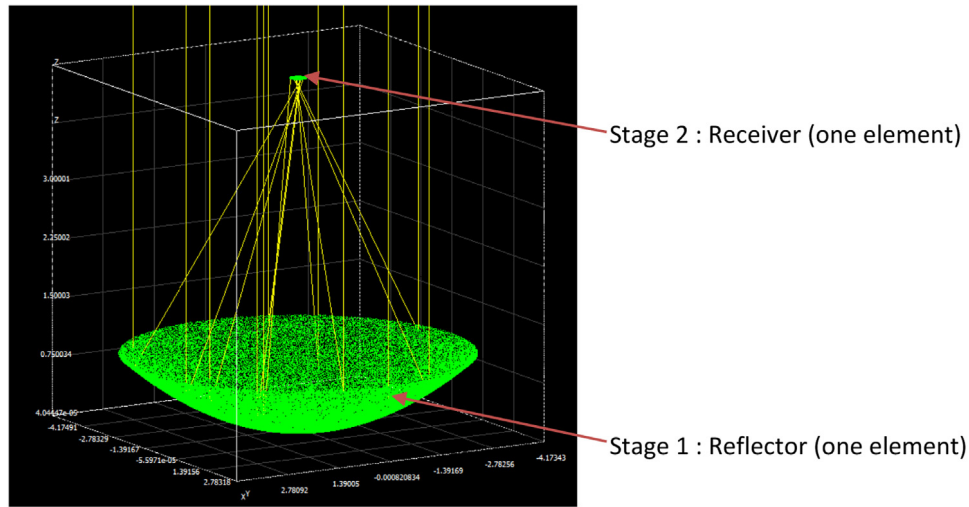


Fig. 2. Schematic of parabolic concentrator.

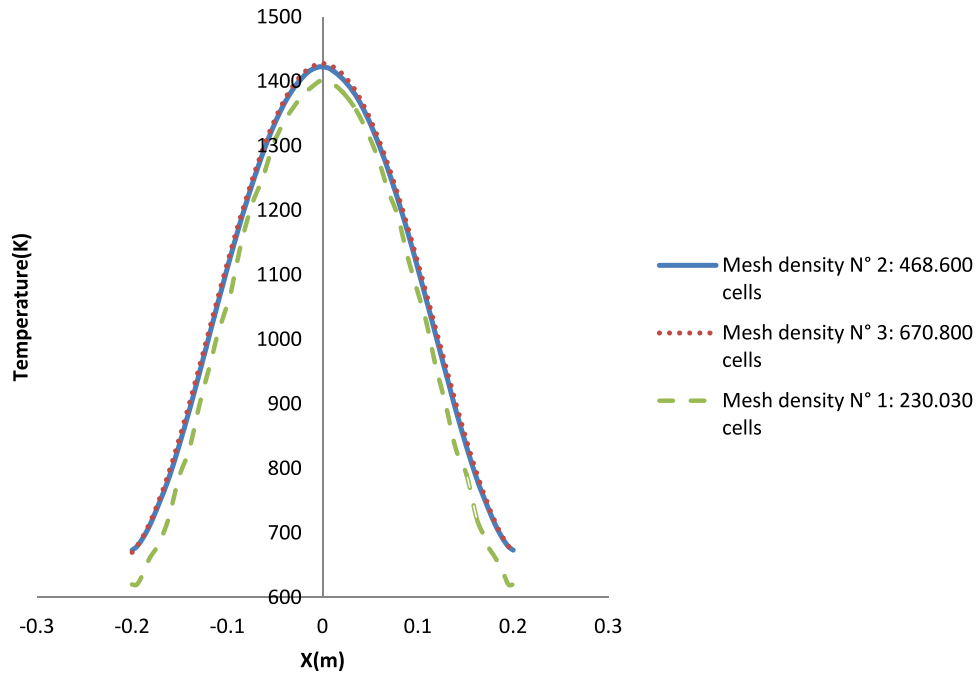


Fig. 3. Numerical temperature profiles of the receiver's tube for different tested grid meshes.

Table 1

Geometric parameters and optical properties of the parabolic dish.

Parabolic dish	Value
Diameter	4.175 m
Focal length	4.5 m
Reflectivity	92%
Transmissivity	8%

2.2. Geometry configuration and mesh

After the determination of the solar heat flux by SOLTRACE, the thermal study of the receiver's dish will be performed using Fluent.

In fact, the geometry of the receiver's dish is created on GAMBIT 2.3. The same dimensions, properties and materials of the configuration (Yu et al., 2015) are introduced for the CFD simulation.

The mesh generated in the geometric model consists of hexahedral cells. A grid independence test is also performed in order to ensure the independence of the numerical results from the grid density.

Three mesh grids are tested: the first with 230.030 nodes, a second with 468.600 and a third grid with 670.800 nodes. Fig. 3 presents the temperature profiles of the receiver's tube using the three tested meshes. The temperature profiles demonstrate that, as the number of nodes increases from 230.030 to 468.600 and from 468.600 to 670.800, the difference between the results decrease respectively from 4.99% to 0.05%. A little change is observed in the results obtained for the second and third mesh (the difference between results is equal to 0.05%). Therefore, the temperature profile of the receiver tube can be properly described using the second grid. For this reason, the number of nodes is chosen equal to 468.600 for the further calculations.

The optimal mesh is, then, exported to the FLUENT software (FLUENT-Inc., 2005) for the resolution.

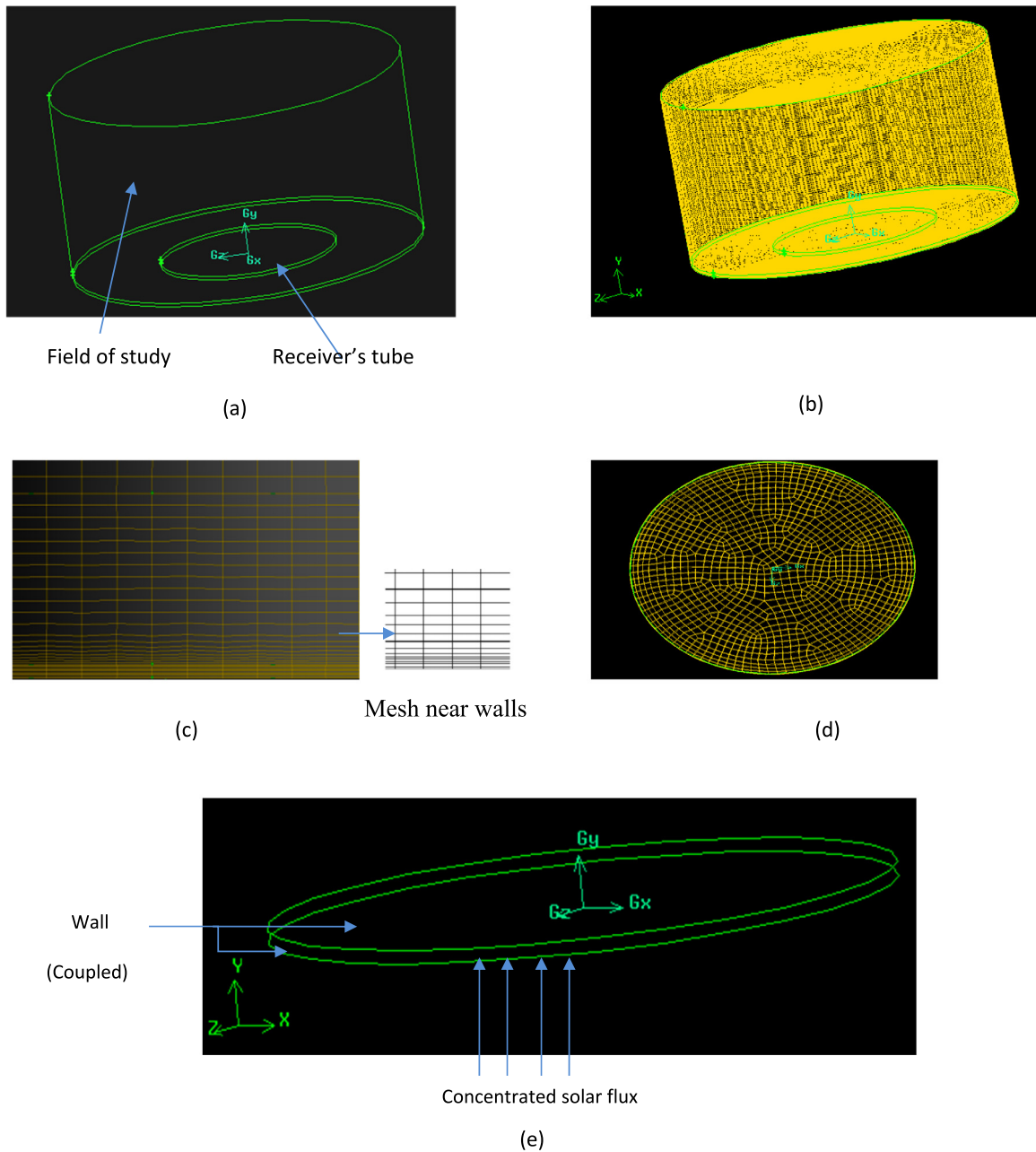


Fig. 4. Mesh details and boundary conditions of the configuration.

The detailed mesh configuration and boundary condition are illustrated in Fig. 4.

The geometry creation of the entire field and its generated mesh are shown in Fig. 4(a) and (b). In Fig. 4(c) and (d), we present precisely the mesh near the wall and in the receiver's plate. The detailed boundary conditions are clearly described in Fig. 4(e).

2.3. Assumptions and boundary conditions

Several assumptions are adopted in order to reduce the complexity of the problem:

- Steady-state flow.
- Incompressible Ideal gas fluid.
- For a temperature range between 300 K and 1000 K, the ambient air properties are treated as a polynomial function of temperature (Bahremand et al., 2015).

- For a temperature range between 300 K and 1700 K, the thermal conductivity and specific heat capacity of the stainless steel are treated as a function of temperature (Bogaard, 1985; Bogaard et al., 1993).

As detailed in Fig. 4, the boundary conditions used when validating the numerical model are as follows:

(a) The plate lateral surface and the absorber lower and higher surfaces are considered as "wall" $u=v=w=0$.

(b) The absorber lower surface exposed to the reflector is subjected to a non-uniform solar heat flux distribution calculated by the SOLTRACE software. The solar heat flux distribution calculation is detailed in Section 3.1.

(c) The heat transfer between the higher and the lateral surfaces of the absorber and the surrounding fluid is specified as a "coupled" wall condition.

In fact, when the wall zone has a fluid or solid region on each side, it is called a "two-sided wall". The two sides of the wall

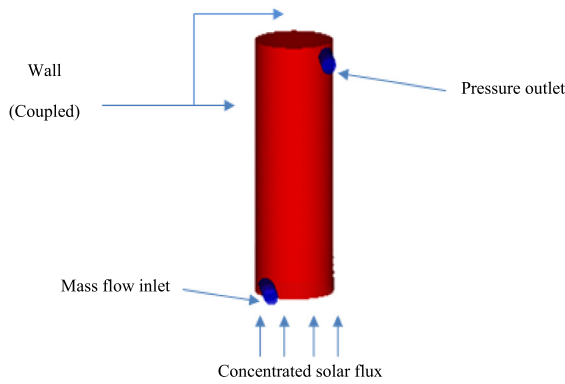


Fig. 5. Details of boundary conditions.

are coupled, using the Coupled option under thermal conditions. The use of this boundary condition allows to perform a heat transfer analysis to predict the operating temperature of each wall, in relation to the flow and thermal state inside and outside the receiver’s wall. No additional thermal boundary conditions are required for this thermal limit because the solver calculates the heat transfer directly from the solution in the adjacent cells. By giving the wall emissivity coefficient, the solver allows to simulate the radiative and convective heat transfer in the receiver surfaces.

For the rest of the studied cases, the boundary conditions used are as follows, and are well detailed in Fig. 5:

(a) The plate lateral surface and the absorber lower and higher surfaces are considered as “wall” $u=v=w=0$.

(b) The absorber lower surface exposed to the reflector is subjected to a non-uniform solar heat flux distribution calculated by the SOLTRACE software. The solar heat flux distribution calculation is detailed in Section 3.1.

(c) The heat transfer between the higher and the lateral surfaces of the absorber and surrounding fluid is specified as a “coupled” wall condition.

(d) The boundary conditions applied to the inlet and outlet of the working fluid are as follows:

Inlet: “mass flow inlet”: this type of condition is considered for an incoming flow.

Outlet: fully developed assumption: $\frac{\partial u}{\partial x} = \frac{\partial v}{\partial x} = \frac{\partial w}{\partial x} = \frac{\partial k}{\partial x} = \frac{\partial \epsilon}{\partial x} = \frac{\partial p}{\partial x} = \frac{\partial T}{\partial x} = 0$

Argon gas is considered the working fluid. Physical properties of the working fluid are treated as a polynomial function of temperature (Lu et al., 2009).

(e) The Reynolds number Re is calculated according to the relation $Re = \frac{\rho v d}{\mu}$. A value of $Re= 22968$ is found. This value is higher than the critical value and corresponds to the turbulent flow.

2.4. CFD numerical simulation

The conservation equations of mass, momentum, energy and species are numerically solved by the FLUENT software. The P1 radiation model is adopted to determine the thermal radiation heat transfer in numerical simulations.

The SIMPLE algorithm is used to solve the pressure–velocity coupling field to satisfy the mass conservation law. The Standard k-epsilon model is used as a turbulence closure model, and is characterized by its acceptable predictions for many flows. The first-order upwind scheme is applied for all equations except for the “momentum” and “energy” which are discretized using the second-order upwind scheme. The convergence criterion choice

is carried out. As 10^{-3} allows to obtain a higher accurate result for the continuity and momentum conservation equations than 10^{-2} where the difference was moved from 4% to 0.1%, it is chosen as convergence criteria. Similarly, 10^{-6} is chosen for the energy and P1 equations.

2.5. Mathematic models of the heat transfer

The governing equations are the Navier–Stokes equations (NSE).

Based on the Favre decomposition and taking into account the simplified assumptions, the conservation equations of mass, momentum and energy are written as follows (Farjallah et al., 2016):

- The continuity equation

$$\frac{\partial}{\partial x_i} (\bar{\rho} \tilde{u}_i) = 0 \tag{1}$$

- The momentum conservation equation

$$\frac{\partial}{\partial x_j} (\bar{\rho} \tilde{u}_i \tilde{u}_j) = -\frac{\partial \bar{p}}{\partial x_i} + \frac{\partial}{\partial x_j} \left[\mu \left(\frac{\partial \tilde{u}_i}{\partial x_j} + \frac{\partial \tilde{u}_j}{\partial x_i} - \frac{2}{3} \delta_{ij} \frac{\partial \tilde{u}_k}{\partial x_k} \right) \right] \tag{2}$$

Where $\frac{\partial}{\partial x_j} (\bar{\rho} \tilde{u}_i \tilde{u}_j)$ is the convective transport term.

- The energy conservation equation

$$\frac{\partial \bar{\rho} \tilde{u}_j \tilde{T}}{\partial x_j} = \frac{\partial}{\partial x_j} \left(\frac{\lambda}{C_p} \frac{\partial \tilde{T}}{\partial x_j} - \overline{\rho u_j T''} \right) + S_h \tag{3}$$

- The P1 model is adopted to consider the thermal radiation in numerical simulations.

The radiation intensity transport equation is presented as follows (FLUENT–Inc., 2005):

$$\nabla \cdot (\Gamma \nabla I) - aI + 4an^2\sigma T^4 = S_g \tag{4}$$

Where $\Gamma = \frac{1}{3*(a+\sigma_s)-C\sigma}$

- I : the incident radiation
- a : the absorption coefficient
- σ_s : the scattering coefficient
- n : the refractive index of the medium
- $\sigma = 5.672 \cdot 10^{-8} \text{ W/m}^2 \text{ K}^4$: the Stefan – Boltzmann constant
- T: la température
- C : the linear – anisotropic phase function coefficient
- S_g : user – defined radiation source

2.6. Thermal study of the inlet/outlet configuration

The inlet/outlet configuration is an important parameter that influences the global performance of the solar parabolic dish that is why the effect of the inlet and outlet positions is studied in this paper for different configurations of the cylindrical receiver. These positions are well detailed in Fig. 6: the tangential inlet located at the top with a tangential outlet located at the bottom, and the tangential inlet located at the bottom with a normal outlet on the top surface.

For the first configuration, the solar receiver is a cylindrical absorber with a 0.4 m diameter and 0.075 m height.

The second configuration is a cylinder with a 0.5 m diameter and 0.048 m height. Thereafter, in the third configuration, the solar receiver configuration consists of a cylinder of a 0.1 m in diameter and 1.2 m in height and the fourth configuration is a cylinder of 0.16 m in diameter and 0.468 m in height.

The solar receiver is made of stainless steel. Argon gas is considered the working fluid that enters the absorber through the inlet at ambient conditions at a constant flow rate and leaves it through the outlet at ambient conditions.

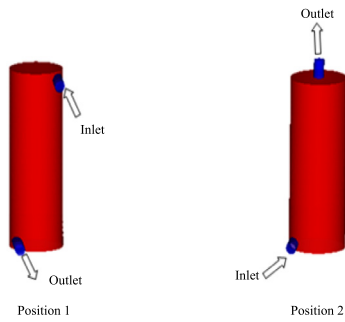


Fig. 6. Different positions studied.

Ambient temperature and pressure are considered 300 K and 101 351 Pa, respectively.

The cylindrical receiver is frequently used in several applications such as low temperature heating, cold production and steam generation.

Table 2 shows the properties of the different studied configurations.

The different receiver configurations investigated and designed in GAMBIT, are given in Fig. 7.

3. Results and discussion

3.1. Validation of solar heat flux distribution

To guarantee the effectiveness of the SOLTRACE software to predict the concentrated solar heat flux distribution in the focal

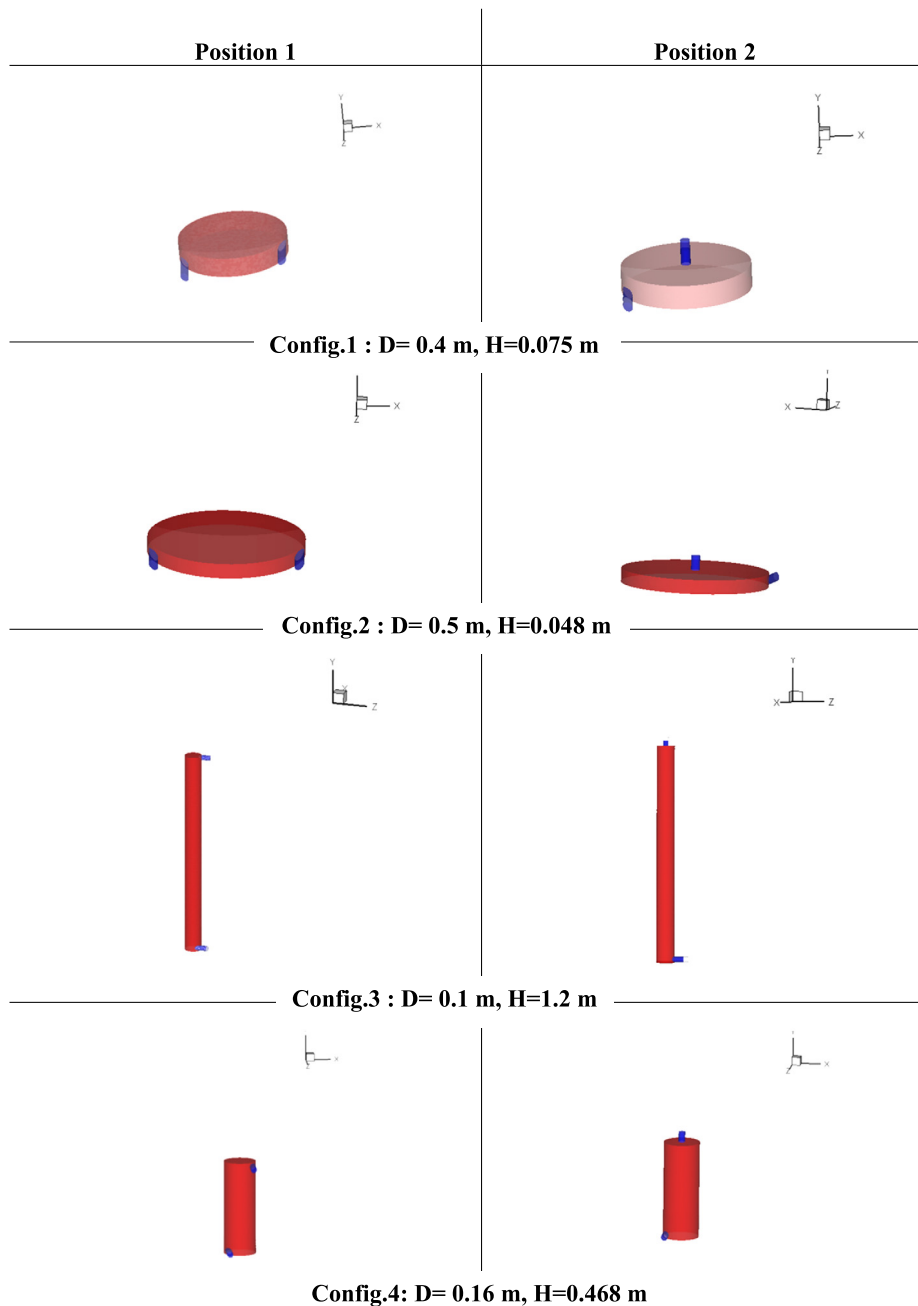


Fig. 7. The different receiver configurations.

Table 2
Geometric properties of the receiver configurations.

Configurations	Geometric properties	
	Diameter (m)	Height (m)
Config. 1	D = 0.4	H = 0.075
Config. 2	D = 0.5	H = 0.048
Config. 3	D = 0.1	H = 1.2
Config. 4	D = 0.16	H = 0.468

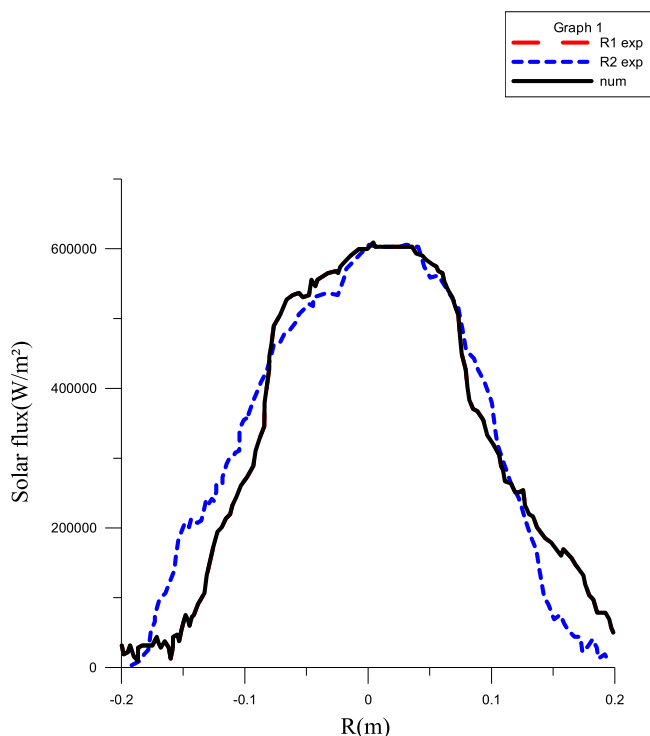


Fig. 8. Comparison between the SOLTRACE code and Yu et al.'s (2015) results of focal flux distribution on a 0.4 m diameter absorber.

point of the receiver, a validation of the model with experimental data is made.

The validation is achieved by comparing the numerical results calculated by SOLTRACE with the experimental data collected by Yu et al. (2015).

We take into account the same assumptions considered by Yu et al. (2015). The heat flux distribution at the focal plane of the parabolic dish is compared with that achieved by Yu et al. (2015), in Fig. 8. We note that a good agreement is obtained between numerical results and Tao Yu's experimental results.

The results are statistically significant with a very high R-squared value (above 0.98763) and very low P -value (in a range of $0 \leq P \leq 2 \times 10^{-8}$) which is equivalent to a percentage average error of 7.94%.

The latter result confirms that the MCRT method used in the present study is feasible and the numerical findings are reliable.

The solar radiation heat flux reaches a peak of about 650,000 W/m² in the central region. The concentrated solar heat flux distribution is shown to reach the focal point rapidly. Outside the central region, the concentrated solar radiation is very low because the receiver tube receives only a direct radiation.

The concentrated solar heat flux distribution calculated by SOLTRACE is shown in Fig. 9.

The surface plot of the concentrated solar heat flux distribution is presented in Fig. 9(a). It is clearly shown that the distribution is symmetric along the plan $X=0$ and the plan $Y=0$.

In Fig. 9(b), the contour plot of this latter is shown. It is conspicuous that the distribution is symmetric along the horizontal and vertical center line. It is noted that the flux is maximum at the center of the receiver and it gradually decreases by moving away from the plate center.

After ensuring the validity of the model on the SOLTRACE software, we can conclude that the MCRT method can be used to predict the concentrated solar heat flux distribution on a receiver located in the focal point of a parabolic dish or in any other solar application.

3.2. Validation of the receiver temperature distribution

In order to validate the heat transfer process of the receiver, a direct normal irradiation of 458.3 W/m², the same direct normal irradiation of Yu et al. (2015), and a Gaussian sun shape are supposed in the SOLTRACE software. Then, the solar heat flux distribution predicted by this software is introduced into the FLUENT software as thermal boundary conditions to the receiver wall through UDF. After that, the results obtained are compared to the experimental results of Yu et al. (2015).

The evolution of the receiver temperature along the horizontal and vertical center line by the FLUENT software is presented in Fig. 10.

It can be seen from this figure that the numerical receiver's temperature is very close and agrees well with Tao's experimental results. It is found that the numerical receiver's temperature results differ from the experimental results of Yu et al. (2015) only by 2.5%.

So, we can prove the validity of the heat transfer process of the receiver.

Fig. 11 depicts the receiver's plate temperature. It is clear that the maximum temperature is at the center of the plate, it reaches 1438 K, and by moving away from the center, the temperature diminishes gradually to attain 670 K. This diminution in temperature is explained by the concentrated solar heat flux distribution. In fact, the concentrated solar radiation reaches its maximum value at the center of the receiver. It attains the focal point rapidly. Then, it gradually decreases outside the central region of the plate because the absorber tube receives only a direct radiation.

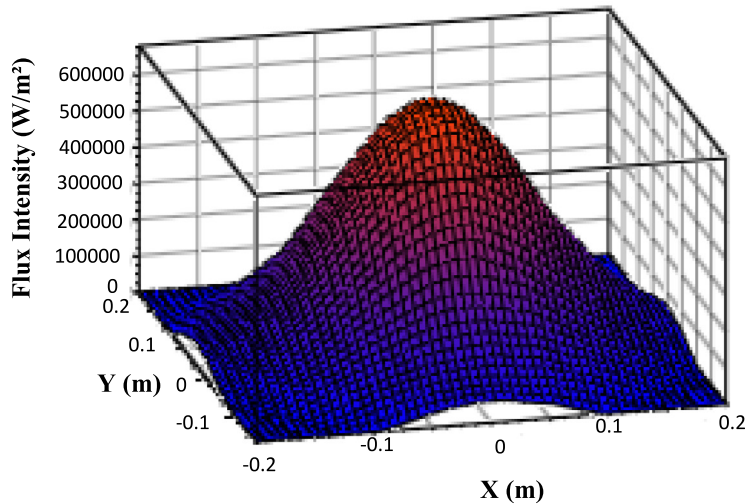
3.3. Effect of the inlet/outlet configuration

The three-dimensional temperature distribution of the different receiver configurations and inlet/outlet positions is shown in Fig. 12 and its outlet temperature distribution is illustrated in Fig. 13.

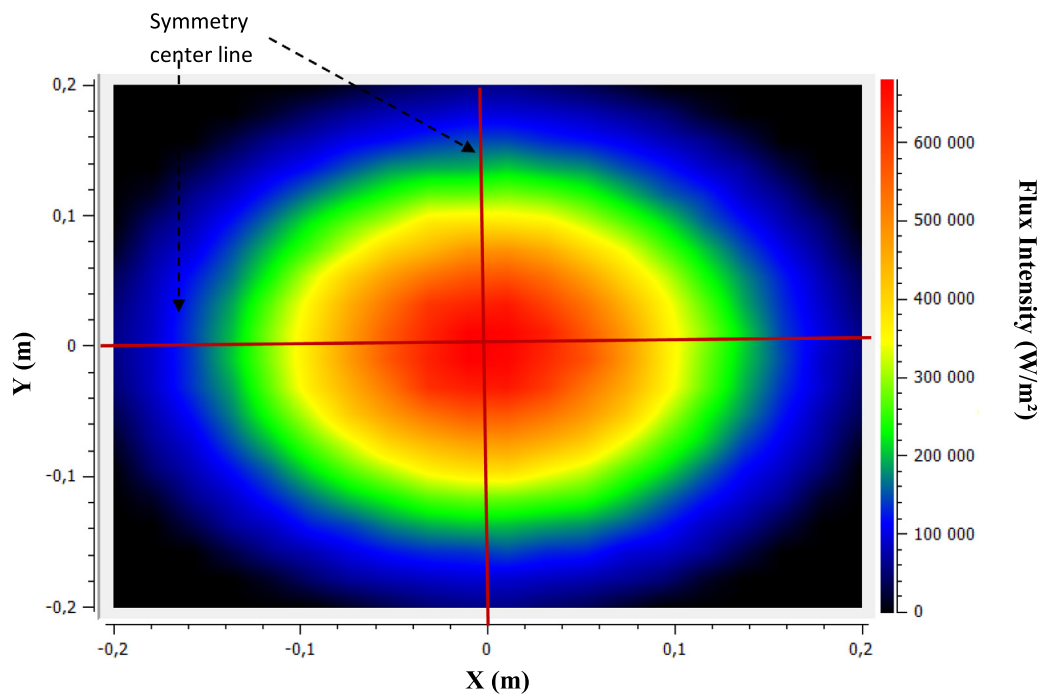
The different inlet/outlet positions are well defined in Table 3.

It can be seen that for the cylindrical absorber Configs. 1 and 2, the temperature of the outlet section for position 2 is higher the one for position 1 (see Fig. 13. Config. 1, Config. 2). Indeed, the outlet fluid temperature of Config. 1 position 2 reaches a maximum of 1000 K whereas for position 1, it reaches a maximum of 930 K. More precisely, the average outlet fluid temperature of the cylindrical absorber (Config. 1 position 1) is equal to 550 K while for position 2, it is about 968 K. Table 4 gives the average outlet fluid temperature of each configuration. It is noted that the average outlet fluid temperature increases by 43% by changing the position from 1 to 2 in config. 1.

Fig. 13 demonstrates that the outlet fluid temperature of position 1 is higher than that of position 2 for the Configs. 3 and 4. In fact, for Config. 4 (position 1), the maximum temperature value is equal to 580 K, while for position 2, the maximum temperature is equal to 460 K.



(a) Surface plot of flux distribution



(b) Contour plot of flux distribution

Fig. 9. The focal flux distribution calculated by SOLTRACE code.**Table 3**
Different inlet/outlet positions.

Position 1	Tangential inlet located at the top with a tangential outlet located at the bottom
Position 2	Tangential inlet located at the bottom with a normal outlet on the top surface

Furthermore, as illustrated in Table 4, the average outlet fluid temperature of Config. 4 position 1 is equal to 493 K but for position 2, it is about 411.3 K. The average outlet fluid temperature decreases by 16.5% by changing the position from 1 to 2 in Config. 4.

Table 5 gives the receiver's wall average temperature for the different configurations and positions. It is observed that for Configs. 1 and 2, the receiver's wall average temperature for

position 1 "Tangential inlet located at the top with a tangential outlet located at the bottom" is greater than that of the receiver's wall for position 2 "Tangential inlet located at the bottom with a normal outlet on the top surface".

The increase of the receiver's wall average temperature implies an increase of heat losses to the environment and subsequently the fluid average temperature decreases. This explains

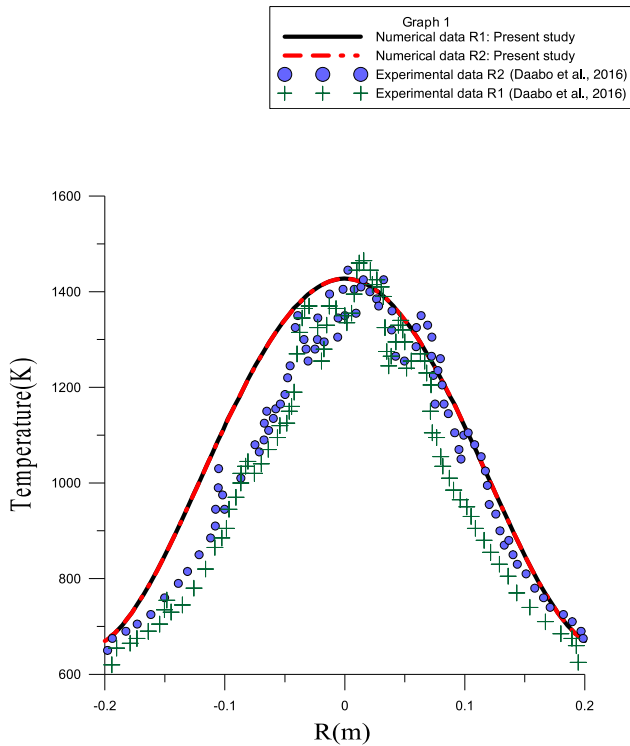


Fig. 10. Comparison between experimental and numerical temperature distribution of the receiver plate.

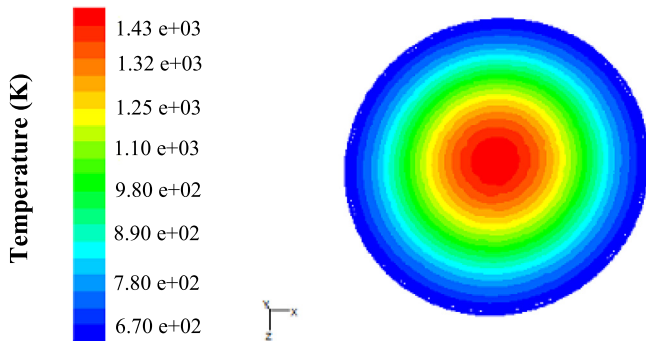


Fig. 11. Temperature of plate receiver.

Table 4
Average outlet fluid temperature of each configuration.

Configuration	Average temperature (K)	
	Position 1	Position 2
Config. 1	550	968
Config. 2	520	826
Config. 3	444	367
Config. 4	493	411.3

Table 5
Receiver wall average temperature.

Configuration	Receiver wall average temperature (K)	
	Position 1	Position 2
Config. 1 : D = 0.4 m, H = 0.075 m	998.4	981.98
Config. 2 : D = 0.5 m, H = 0.048 m	844.42	820.8
Config. 3 : D = 0.1 m, H = 1.2 m	375.3	401.3
Config. 4: D = 0.16 m, H = 0.468 m	502.7	510.7

Table 6
Receiver thermal efficiency.

Configuration	Receiver thermal efficiency η_{th} (%)	
	Position 1	Position 2
Config. 1 : D = 0.4 m, H = 0.075 m	2.65	7.09
Config. 2 : D = 0.5 m, H = 0.048 m	1.5	3.57
Config. 3 : D = 0.1 m, H = 1.2 m	24.48	11.4
Config. 4: D = 0.16 m, H = 0.468 m	12.8	7.4

that the fluid average temperature for position 2 is greater than that of position 1 for Configs. 1 and 2.

Table 5 shows also that, for Configs. 3 and 4, the receiver's wall average temperature for position 1 is smaller than that of the receiver's wall for position 2. The decrease of the receiver's wall average temperature implies a decrease of heat losses to the environment, and subsequently the fluid average temperature increases. This explains that the fluid average temperature for position 1 is greater than that of position 2.

In Fig. 14, we represent the streamlines of the fluid in the receiver to better explain this phenomenon.

The streamlines of the first configuration (Config. 1 (position 1)), plotted in Fig. 14(a), indicate that the flow of heat transfer fluid passes through the middle of the receiver away from the receiving inner section of the solar flux. Therefore, the fluid flow does not absorb a large amount of heat. In addition, for the lowest cylinder height (H = 0.075 m), the output section is very close to the input section. The fluid flow passes directly through the outlet section without absorbing maximum heat.

On the other hand, for the first configuration (Config. 1 (position 2)), the fluid flow entering through the inlet section intercepts the lower surface which receives the concentrated solar flux, and therefore, it heats up more. The exit section is located in the middle of the upper face of the cylinder which is in front of the focal point of the parabolic dish. As illustrated in Figs. 14(d) and (e), the fluid flow is found to pass through the focal spot which is the hottest area before it passes through the outlet section, and therefore, it absorbs more heat and subsequently its average outlet temperature is higher than that of the first configuration (Config. 1 (position 1)).

Fig. 15 represents the temperature and flow streamlines of the fourth configuration (Config. 4 (position 1)). It can be seen that the flow gets decelerated soon after it has passed through the inlet section. In addition, we note that the flow undergoes the effects of inertia and buoyancy. The maximum fluid velocities are higher in the outer section than in the inner section of the receiver as illustrated in Fig. 15(c). This result indicates that the swirling effects are significant. The velocity magnitudes are stronger in the region close to the outlet, which indicates that the buoyancy-driven flow is superimposed on the velocity field.

The large variation in velocities indicates a variation of the fluid temperature. Therefore, the average outlet fluid temperature reaches 493 K.

For Config. 4 (position 2) (see Fig. 16(a)), it is noted that the temperature distribution is almost uniform in the upper two-thirds of the receiver and variable in the lower part. The velocity field in the central region is very small as illustrated in Fig. 16(b);

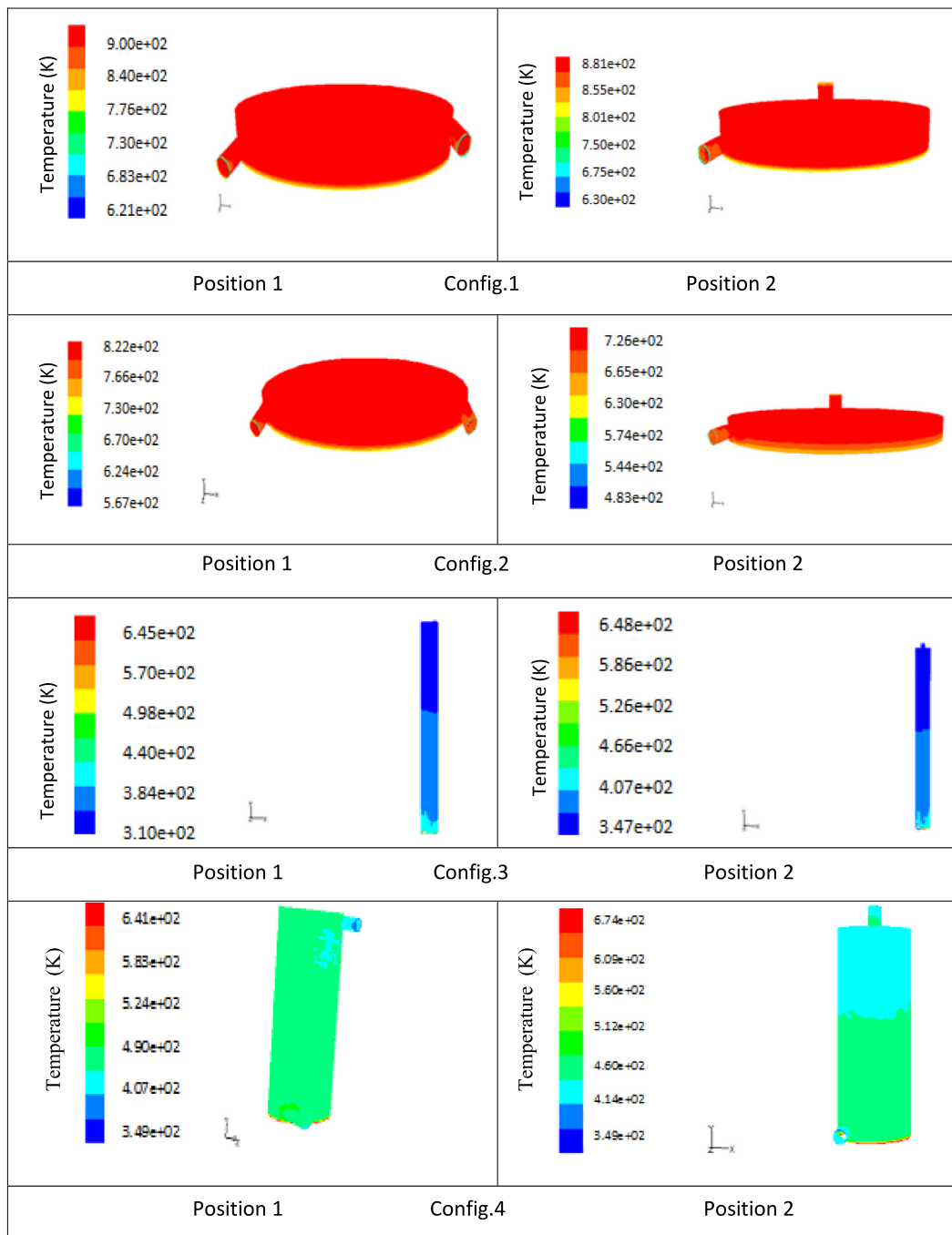


Fig. 12. The temperature distribution of the different receiver configurations.

it reaches its maximum in the region near the outlet section. The fluid velocity magnitude corresponding to Config. 4 (position 2) is small compared to that of Config. 4 (position 1). Thereafter, its average outlet temperature is low compared to Config. 4 (position 1).

Table 6 gives the receiver thermal efficiency for the different tested configurations and for the two inlet/outlet fluid positions (position 1 and 2).

The receiver thermal efficiency is defined as follows (Lee et al., 2016)

$$\eta_{th} = \frac{\dot{m}C_p(T_{out} - T_{in})}{C_s I A_s} \quad (5)$$

Where, A_s and \dot{m} are respectively surface area of receiver and mass flow rate of working fluid.

It can be seen that for the cylindrical absorbers Configs. 1 and 2, the thermal efficiency of position 2 is higher the one for position 1.

Indeed, for Config. 1, the thermal efficiency corresponding to position 2 is about 7.09% whereas for position 1, it is about 2.65%. It has been shown that the thermal efficiency increases by 62.6% by changing the position from 1 to 2 in Config. 1. It is observed that position 2 gives the greatest thermal efficiency for these two tested configurations Configs. 1 and 2.

The thermal efficiency of position 1 is higher than that of position 2 for the Configs. 3 and 4. In fact, for Config. 3 (position 1), the thermal efficiency value is equal to 24.48%, while for position 2, it is equal to 11.4%. It is noted that the thermal efficiency decreases by 53% by changing the position from 1 to 2 in Config.

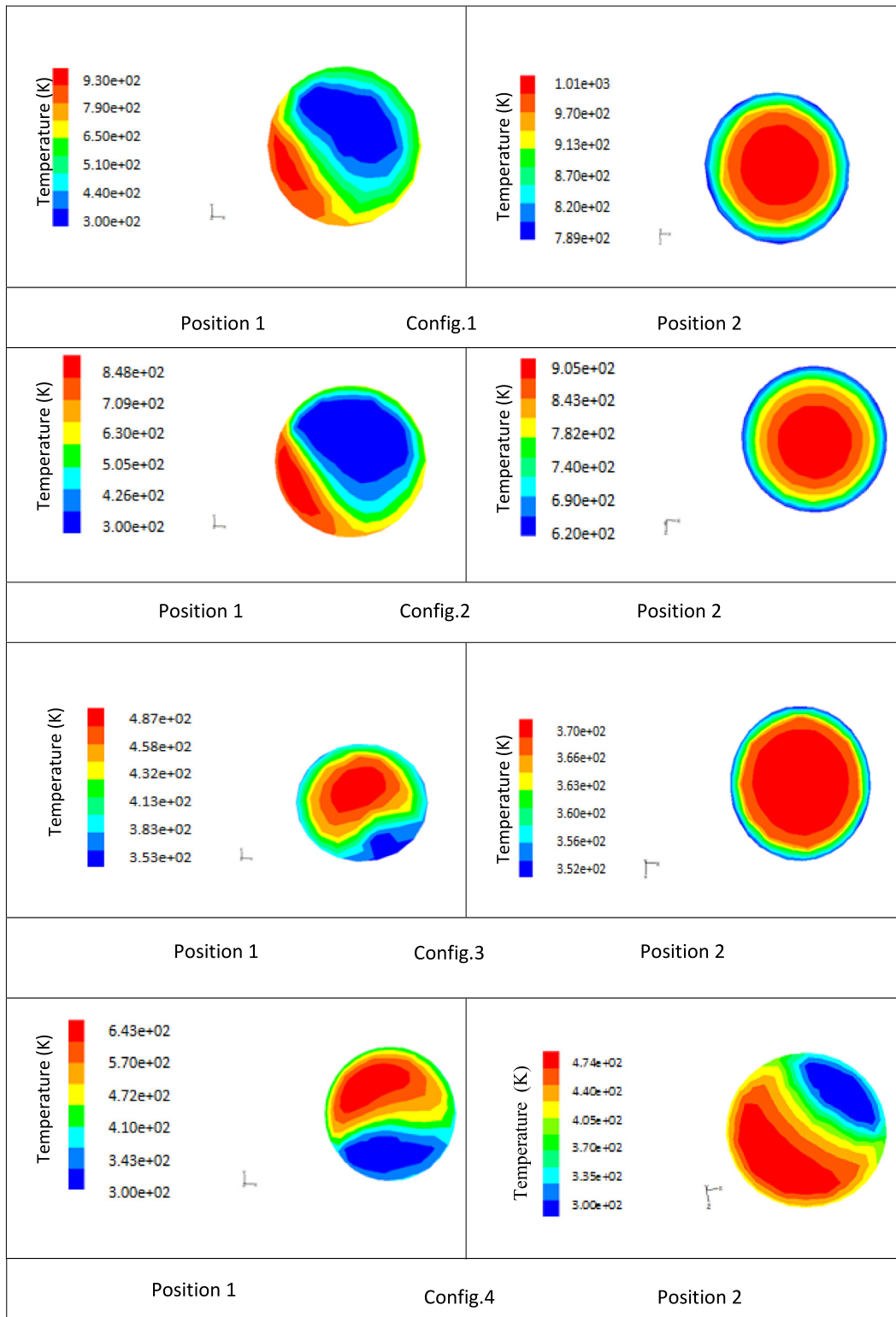


Fig. 13. The outlet temperature of different receiver configurations.

3. This result indicates that position 1 ensures the best thermal efficiency for these two configurations Configs. 3 and 4.

In Table 7, we represent the thermal efficiency for the different tested configurations for the two inlet/outlet positions.

The present study demonstrates that the results of Wang and Siddiqui (2010) are not validated for all aspect ratios of the receiver. In fact, Wang and Siddiqui (2010) has tested specified geometric dimensions of the receiver (a fixed aspect ratio) and

several fluid inlet/outlet configurations. Mo Wang has concluded that the configuration of the tangential inlet located at the top with a tangential outlet located at the bottom is the configuration that ensures the best thermal performance.

In our study, we have tested different geometric dimensions of the receiver. We demonstrate that, for the “elevated” height cylindrical receiver, the greatest thermal efficiency value corresponds to the configuration of a tangential inlet located at the

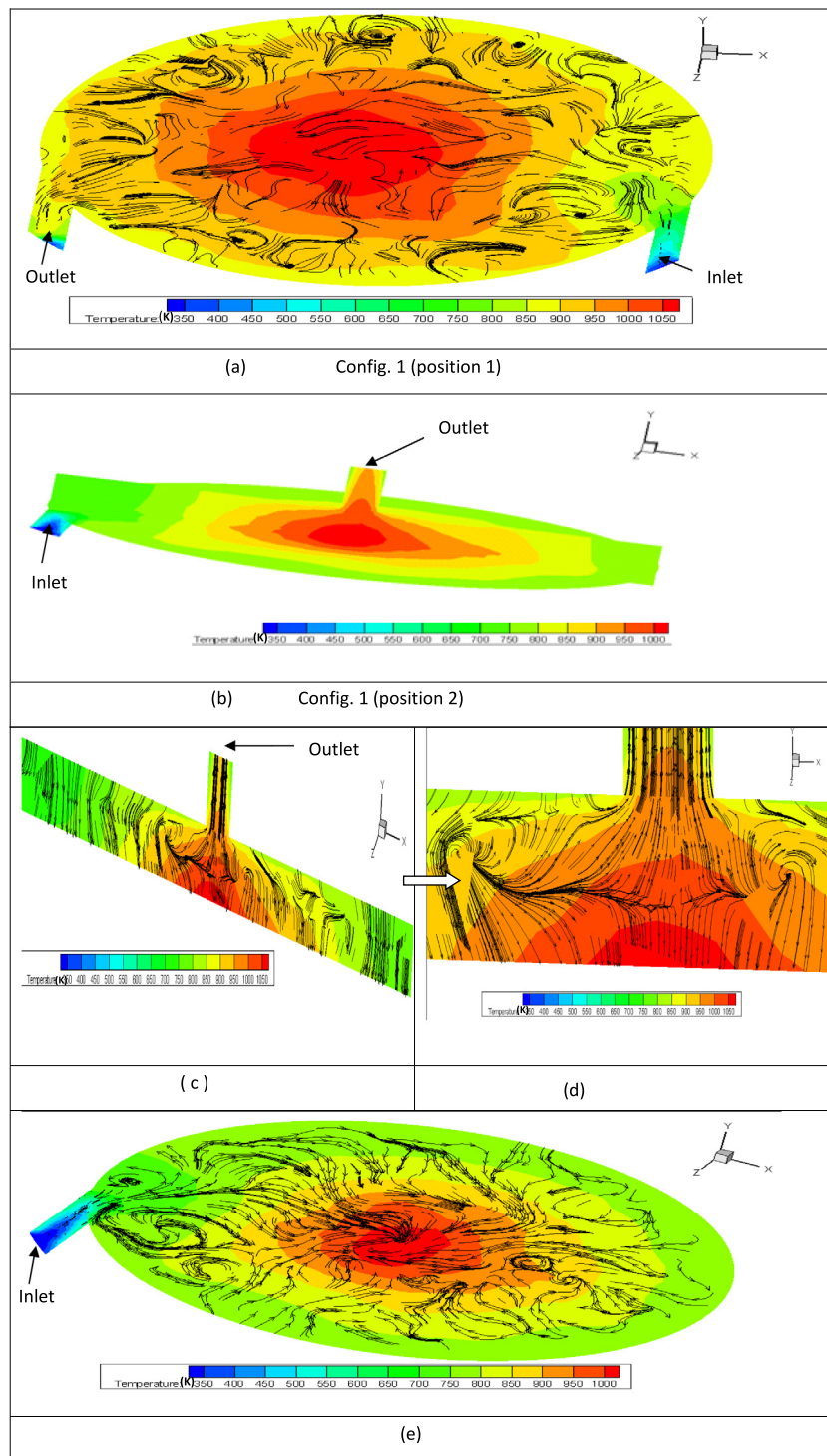


Fig. 14. The temperature streamlines of Config. 1.

top with a tangential outlet located at the bottom, similarly to the result of Mo Wang.

But for a lower height receiver, the results of Mo Wang are not confirmed and the best thermal configuration is reached when the tangential inlet is located at the bottom and the normal outlet is located on the top surface of the receiver.

Conclusions

This paper presents a numerical study of the radiation flux and temperature distributions on the receiver's surface of a parabolic

dish. The SOLTRACE code is used to study the radiation flux distribution and the FLUENT software to investigate the temperature distribution.

A comparison between our numerical results and experimental results of Yu et al. (2015) is done and a good agreement is obtained confirming the validity of our numerical method.

Two inlet/outlet configurations are investigated for four cylindrical receivers in order to verify the result of Mo Wang for all aspect ratios of the receiver (Diameter/Height) by keeping the same cylinder volume of Mo Wang.

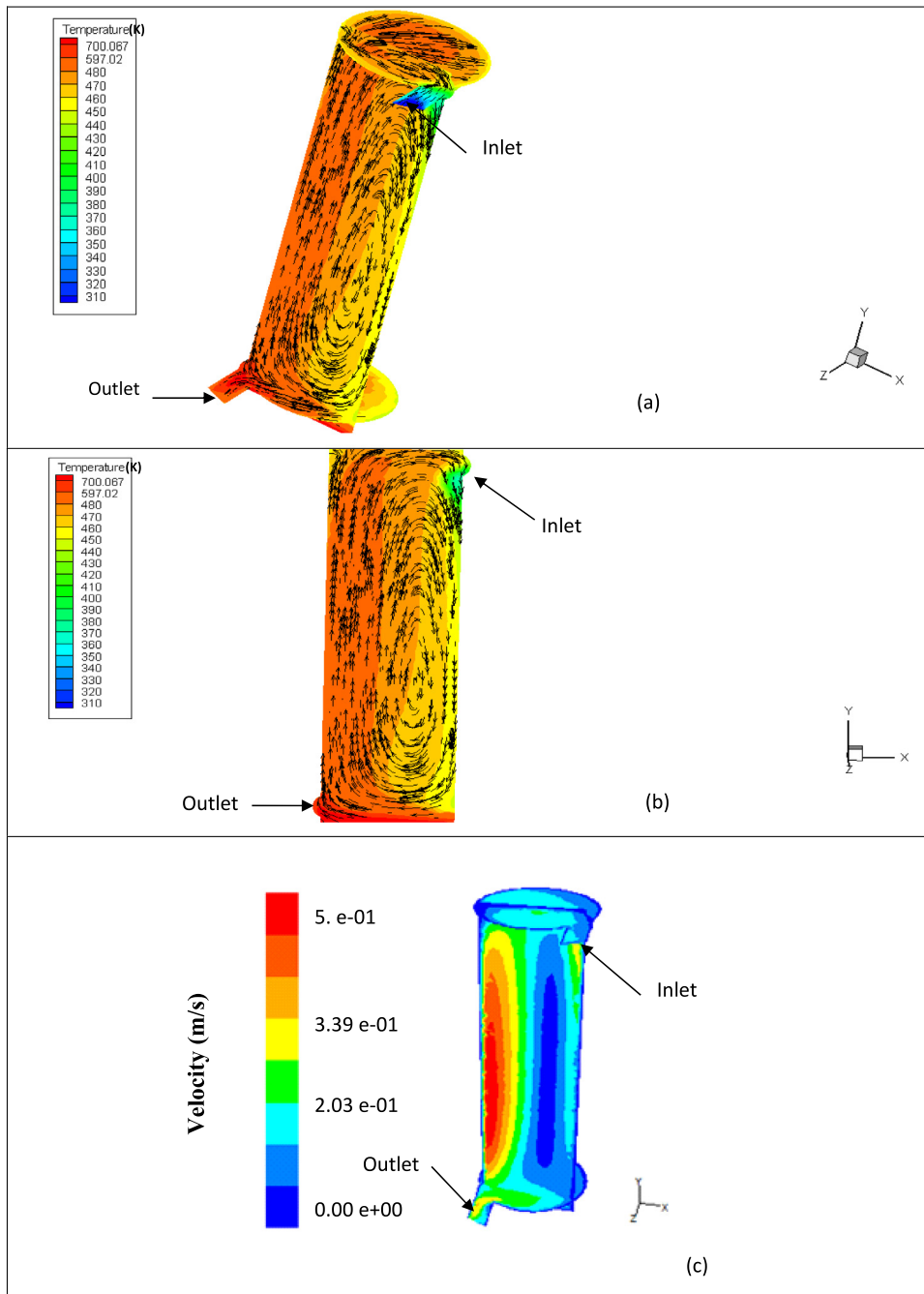


Fig. 15. The temperature and flow streamlines of Config. 4 (position 1).

Table 7
The obtained results.

	Position 1	Position 2
Config. 1 : D = 0.4 m, H = 0.075 m		Thermal efficiency (Position 1) < Thermal efficiency (Position 2)
Config. 2 : D = 0.5 m, H = 0.048 m		Thermal efficiency (Position 1) < Thermal efficiency (Position 2)
Mo Wang Configuration: D = 0.2 m, H = 0.3 m		Thermal efficiency (Position 1) > Thermal efficiency (Position 2)
Config. 3 : D = 0.1 m, H = 1.2 m		Thermal efficiency (Position 1) > Thermal efficiency (Position 2)
Config. 4: D = 0.16 m, H = 0.468 m		Thermal efficiency (Position 1) > Thermal efficiency (Position 2)

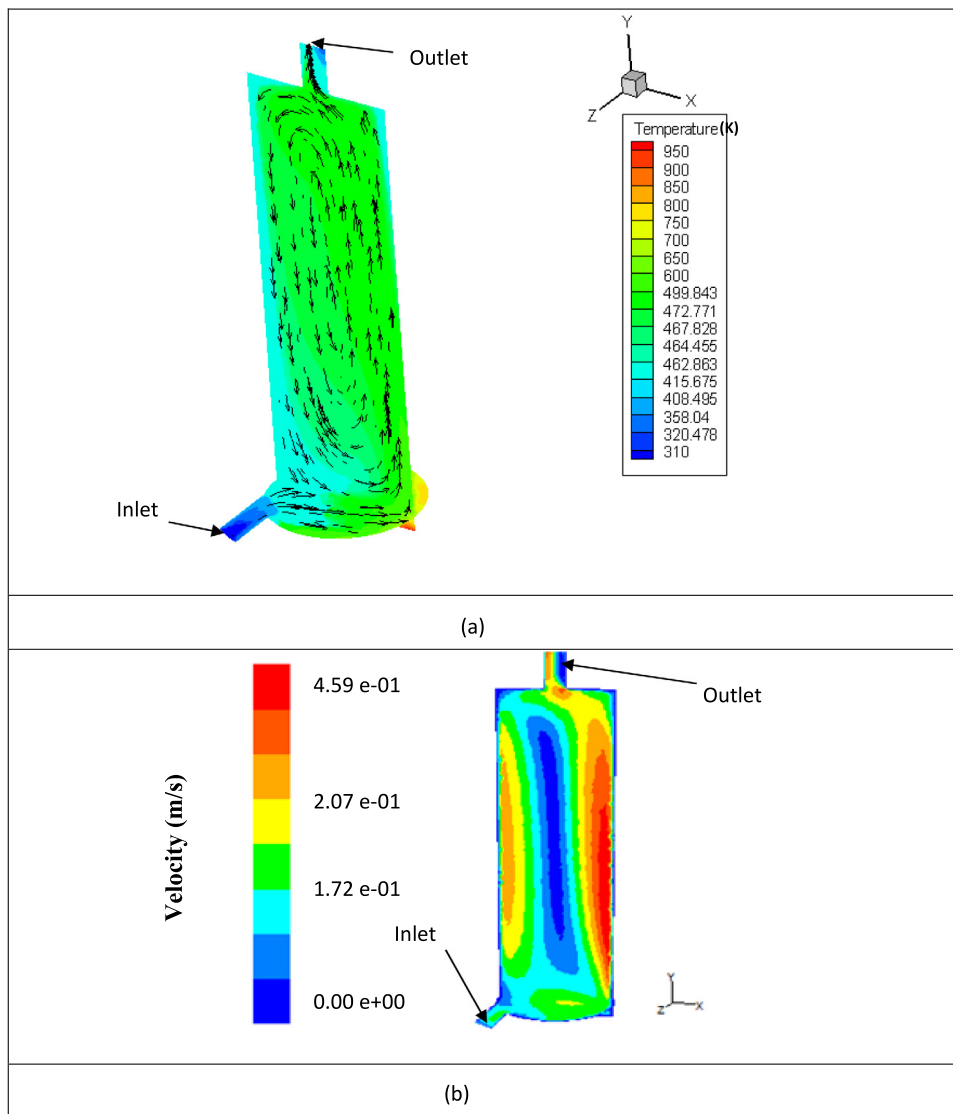


Fig. 16. The temperature and flow streamlines of Config. 4 (position 2).

The simulation results clearly showed that the outcome of Mo Wang is not validated for all aspect ratios of the receiver. The optimal thermal performance of the parabolic dish depends on the geometric properties of the receiver and on the inlet/outlet positions. In fact,

- With a “low” height cylindrical receiver ($H=0.075$ m, $H=0.048$ m), position 2 of a tangential inlet located at the bottom with a normal outlet on the top surface is the best configuration achieving the optimal system performance. Really, the thermal efficiency increases by 62.6% by changing the position from 1 to 2 with $H=0.075$ m.
- With an “elevated” height cylindrical receiver ($H=1.2$ m, $H=0.468$ m), position 1 of a tangential inlet located at the top with a tangential outlet located at the bottom is the most beneficial position for this solar application. Indeed, the thermal efficiency decreases by 53% from position 1 to 2 for a configuration with $H=1.2$ m.

References

Azzouzi, D.I., Boumeddane, B., Abene, A., 2017. Experimental and analytical thermal analysis of cylindrical cavity receiver for solar dish. *Renew. Energy* <http://dx.doi.org/10.1016/j.renene.2016.12.102>.

- Badran, A.A., Yousef, I.A., Joudeh, N.K., Al Hamad, R., Halawa, H., Hassouneh, H.K., 2010. Portable solar cooker and water heater. *Energy Convers. Manage.* 51 (8), 1605–1609.
- Bahrehmand, D., Ameri, M., Gholampour, M., 2015. Energy and exergy analysis of different solar air collector systems with forced convection. *Renew. Energy* 83, 1119–1130.
- Bogaard, R.H., 1985. Thermal conductivity of selected stainless steels. In: Ashworth, T., Smith, D.R. (Eds.), *Thermal Conductivity 18*, Proceedings of the Eighteenth International Conference on Thermal Conductivity. Plenum, New York, pp. 175–185.
- Bogaard, R.H., Desai, P.D., Li, H.H., Ho, C.Y., 1993. Thermophysical properties of stainless steels. *Thermochim. Acta* 218, 373–393.
- Collado, F.J., Gomez, A., Turegano, J.A., 1986. An analytic function for the flux density due to sunlight reflected from a heliostat. *Sol. Energy* 37, 215–234.
- Daabo, A.M., Mahmoud, S., Al-Dadah, R.K., 2016. The effect of receiver geometry on the optical performance of a smallscale solar cavity receiver for parabolic dish applications. *Energy* 114, 513–525.
- Daly, J.C., 1979. Solar concentrator flux distribution using backward tracing. *Appl. Opt.* 18 (15), 2696–2700.
- Farjallah, R., Chaabane, M., Mhiri, H., Bournot, P., Dhaouadi, H., 2016. Thermal Performance of the U-Tube Solar Collector using Computational Fluid Dynamics Simulation, vol. 138, pp. 1–8.
- FLUENT–Inc., 2005. *FLUENT 6.2 User's Guide*, FLUENT, Inc, FLUENT 6.3 Documentation.
- Furler, P., Scheffe, J.R., Steinfeld, A., 2012. Syngas production by simultaneous splitting of H_2O and CO_2 via ceria redox reactions in a high-temperature solar reactor. *Energy Environ. Sci.* 5 (3), 6098–6103.

- Garcia, P., Ferriere, A., Bezian, J.-J., 2008. Codes for solar flux calculation dedicated to central receiver system applications: A comparative review. *Sol. Energy* 82, 189–197.
- Ghomrassi, A., Mhiri, H., Bournot, P., 2015. Numerical study and optimization of parabolic trough solar collector receiver tube. *J. Sol. Energy Eng.* 137, 1–10.
- Huang, W., Yu, L., 2018. Development of a new flux density function for a focusing heliostat. *Energy* 151, 358–375.
- Huang, W., Yu, L., Hu, P., 2018. An analytical solution for the solar flux density produced by a round focusing heliostat. *Renew. Energy* <http://dx.doi.org/10.1016/j.renene.2018.11.007>.
- Jafrancesco, D., Cardoso, Joao P., Mutuberia, A., Leonardi, E., Les, I., Sansoni, P., Francini, F., Fontani, D., 2018. Optical simulation of a central receiver system: Comparison of different software tools. *Renew. Sustain. Energy Rev.* 94, 792–803.
- Johnston, G., 1998. Focal region measurements of the 20 m² tiled dish at the Australian national university. *Sol. Energy* 63, 117–124.
- Khanna, S., Kedare, S.B., Singh, S., 2013. Analytical expression for circumferential and axial distribution of absorbed flux on a bent absorber tube of solar parabolic trough concentrator. *Sol. Energy* 92, 26–40.
- Khanna, S., Sharma, V., 2015. Effect of number of supports on the bending of absorber tube of parabolic trough concentrator. *Energy* 93, 1788–1803.
- Khanna, S., Sharma, V., 2016. Explicit analytical expression for solar flux distribution on an undeflected absorber tube of parabolic trough concentrator considering sun-shape and optical errors. *Sol. Energy Eng.* 138, 011010-1.
- Khanna, S., Sharma, V., Singh, S., Kedare, S.B., 2016. Explicit expression for temperature distribution of receiver of parabolic trough concentrator considering bimetallic absorber tube. *Appl. Therm. Eng.* 103, 323–332.
- Lee, S.H., Choi, T.J., Jang, S.P., 2016. Thermal efficiency comparison: Surface-based solar receivers with conventional fluids and volumetric solar receivers with nanofluids. *Energy* 115, 404–417.
- Li, Z., Tang, D., Du, J., Li, T., 2011. Study on the radiation flux and temperature distributions of the concentrator-receiver system in a solar dish/stirling power facility. *Appl. Therm. Eng.* 31 (10), 1780–1789.
- Lu, S., Dong, W., Li, D., Li, Y., 2009. Numerical study and comparisons of gas tungsten arc properties between argon and nitrogen. *Comput. Mater. Sci.* 45, 327–335.
- Luo, Y., Lu, T., Du, X., 2018. Novel optimization design strategy for solar power tower plants. *Energy Convers. Manage.* 177, 682–692.
- Mills, D., 2004. Advances in solar thermal electricity technology. *Sol. Energy* 76 (1–3), 19–31.
- Reddy, K.S., Veershetty, G., Srihari Vikram, T., 2016. Effect of wind speed and direction on convective heat losses from solar parabolic dish modified cavity receiver. *Sol. Energy* 131, 183–198.
- Roldan, M.I., Valenzuela, L., Zarza, E., 2013. Thermal analysis of solar receiver pipes with superheated steam. *Appl. Energy* 103, 73–84.
- Sarwar, J., Georgakis, G., Kouloulis, K., Kakosimos, K.E., 2015. Experimental and numerical investigation of the aperture size effect on the efficient solar energy harvesting for solar thermochemical applications. *Energy Convers. Manage.* 92, 331–341.
- Sharma, V., Khanna, S., Nayak, J.K., Kedare, S.B., 2016. Effects of shading and blocking in compact linear fresnel reflector field. *Energy* 94, 633–653.
- Shuai, Y., Xia, X.L., Tan, H.P., 2008. Radiation performance of dish solar concentrator/ cavity receiver systems. *Sol. Energy* 82, 13–21.
- Shuai, Y., Xia, X., Tan, H., 2010. Numerical simulation and experiment research of radiation performance in a dish solar collector system. *Front. Energy Power Eng.* 4 (4), 488–495.
- Steinfeld, A., Schubnell, M., 1993. Optimum aperture size and operating temperature of a solar cavity-receiver. *Sol. Energy* 50, 19–25.
- Tan, Y., Zhao, L., Bao, J., Liu, Q., 2014. Experimental investigation on heat loss of semi-spherical cavity receiver. *Energy Convers. Manage.* 87, 576–583.
- Wang, F., Shuai, Y., Yuan, Y., Liu, B., 2012. Effects of material selection on the thermal stresses of tube receiver under concentrated solar irradiation. *Mater. Des.* 33, 284–291.
- Wang, M., Siddiqui, K., 2010. The impact of geometrical parameters on the thermal performance of a solar receiver of dish-type concentrated solar energy system. *Renew. Energy* 35, 2501–2513.
- Wendelin, T., Dobos, A., Lewandowski, A., 2013. *SolTrace: A Ray-Tracing Code for Complex Solar Optical Systems*, NREL/TP-5500-59163, vol. 15013. National Renewable Energy Laboratory, Denver, Colorado, USA.
- Yu, T., Yuan, Q.Y., Lu, J.F., Ding, J., Lu, Y.L., 2015. Thermochemical storage performances of methane reforming with carbon dioxide in tubular and semi-cavity reactors heated by a solar dish system. *Appl. Energy* <http://dx.doi.org/10.1016/j.applenergy.2015.10.131>.
- Zhang, D., Mu, S., Chan, C.C., You Zhou, G., 2018. Optimization of renewable energy penetration in regional energy system. *Energy Procedia* 152, 922–927.